

System Identification of a GNSS Receiver's RF Filter Impulse Response Function

by Mark L. Psiaki and Brady W. O'Hanlon
Cornell University, Ithaca, N.Y. 14853-7501, U.S.A.

BIOGRAPHIES

Mark L. Psiaki is a Professor of Mechanical and Aerospace Engineering. He received a B.A. in Physics and M.A. and Ph.D. degrees in Mechanical and Aerospace Engineering from Princeton University. His research interests are in the areas of GNSS technology and applications, spacecraft attitude and orbit determination, and general estimation, filtering, and detection.

Brady W. O'Hanlon is a graduate student in the School of Electrical and Computer Engineering. He received a B.S. in Electrical and Computer Engineering from Cornell University. His interests are in the areas of GNSS technology and applications, GNSS security, and space weather.

ABSTRACT

Techniques are developed to identify the net complex envelop impulse response function of a GNSS receiver's RF filters by comparing received and theoretical PRN code auto-correlation functions. This impulse response function can be used to accurately characterize PRN code distortion in a GNSS receiver for purposes of designing advanced signal processing algorithms. Such algorithms might be used in a narrow-band spoofing detector based on P(Y) code signals or in a narrow-band delay-lock loop discriminator that mitigates multi-path effects. The RF filter system identification calculations begin by computing the distorted cross-correlation between an exact replica PRN code and the received signal, as is done in a typical delay-lock loop (DLL). Many more code offsets are used than for a typical DLL, on the order of hundreds, and this off-line calibration procedure may average minutes worth of accumulation data in order to deduce highly accurate measures of the distorted cross-correlation. The distorted cross-correlation is equated to a convolution of the unknown impulse response function with the known undistorted PRN code autocorrelation function. The use of this relationship at many code offsets provides sufficient observability to estimate the nodal coefficients in a spline model of the desired impulse response function. Experimental tests of this technique have been conducted on two receiver types. The test results exhibit good self-consistency of the

modeled distortions of multiple signals received by the same RF front-end. They also agree reasonably well with manufacturer data sheets for the RF front-end filters.

INTRODUCTION

GPS and other GNSS receivers process CDMA spread-spectrum signals by using models of the received versions of their PRN codes. Simple Delay-Lock Loop (DLL) correlators and discriminators presume that the received spread-spectrum signal is identical to the original BPSK-, BOC-, or AltBOC-modulated code. Thus, the impact of band-pass filtering in the receiver's RF front-end is often ignored. When not ignored, this impact is often accounted for by using calibrated distortions of the received correlation function, with a different calibration needed for each different PRN code.

In some applications, this approach to dealing with RF front-end distortion is insufficient. For example, the use of long spreading codes creates a situation where it is impractical to pre-calibrate the distortion for each subsection of the code that might be used to form a correlation accumulation. In the application of Ref. 1, pre-calibration is virtually impossible because knowledge is needed of the actual distorted time histories of packets of about 20 P-code chips at the output of a narrow-band RF front end. There are too many unique packets to calibrate, 5.24×10^6 possible combinations. Furthermore, precise data-based calibration using the encrypted P(Y) code would be very difficult and expensive for civilian receivers.

System identification of the RF filter's envelop impulse response function ² provides a practical alternative to calibration. Knowledge of the impulse response function can be used to mathematically predict the shape of the distorted PRN code chips at the output of an RF front-end. It can also be used to predict the distortion of the cross-correlation between the received code and the original wide-band code. In fact, the latter relationship lies at the heart of the system identification calculations that this paper uses to estimation the RF filter impulse response function.

System identification of RF filter impulse response has been considered by other researchers in their efforts to develop receiver signal processing techniques that

mitigate multi-path effects^{3,4,5,6}. The general goal of these efforts has been to characterize the entire transmission channel from the satellite to the antenna and through the RF front-end. This characterization includes both multi-path effects and the RF filter effects, with emphasis placed on the multi-path effects. The overall goal is to use the channel estimates in order to remove the multi-path effects from the resulting pseudorange data. Therefore, these efforts seek methods that can operate in real-time and that can be applied independently to different satellite signals. References 3 and 6 model the RF filter effects as being those of a simple "brick-wall" filter that passes everything within a certain band with zero attenuation and that completely attenuates everything outside this band. In this case, the filter part of each channel impulse response function is known a priori to be a *sinc* function. References 4 and 5 do not make assumptions about the RF filter. Instead, they use frequency-domain system identification techniques, including Weiner filtering, and they use the known wide-band broadcast PRN codes as the test inputs. Special efforts are made to compensate for the zero input power of CDMA signals at certain frequencies and for the near-zero power near these frequencies. For example, BPSK-encoded signals have zero power at their chipping frequency and multiples thereof. The resulting channel models consists of estimated complex-valued frequency responses at a grid of frequency points. If desired, a time-domain impulse response can be computed by performing an inverse Fourier transform.

Like Refs. 4 and 5, the present paper seeks to determine RF filter impulse response functions by applying system identification techniques to actual RF data, but the previous techniques differ from those developed here in several significant ways. First, the present goal is to characterize only the RF filter's contribution to the channel. The target application is to model the distortion to the 20.46 MHz bandwidth P(Y) code upon passing through an RF filter with a bandwidth of about 2.5 MHz¹. The spectrum plot in Fig. 1 depicts the extreme narrowing of the P(Y) signal bandwidth in this case, which obviously also results in extreme signal distortion. Therefore, the characteristics of the receiver's filter are the dominant concern, and the effects of multi-path are less important in this application. Characterization of the RF filter can be performed once in an off-line calculation that applies for all PRN codes. The system identification calculations can combine the signals from multiple PRN codes in the same calculation, thereby increasing the accuracy and reducing any stray multi-path effects.

Note, however, that the results of such a

system identification can have benefits for multi-path mitigation systems. They can provide the filter part of the real-time channel response function so that the mitigation calculations can focus in estimating the reflected signal properties. Thus, the present work will allow the mitigation techniques in Refs. 3 and 6 to relax their assumptions of *sinc* filter impulse response functions by replacing the *sinc* functions with filter impulse response functions calculated off-line using the techniques of the present paper.

A second difference of the present work from Refs. 4 and 5 is its use of time-domain system identification calculations. Instead of working with complex frequency response phasors at FFT frequency grid points, it works with complex spline node parameters of a splined-model of the time-domain envelop filter impulse response. The number of spline nodes and the number of parameters per node are kept small by design. This forces a certain smoothness on the impulse response function a priori, with corresponding implicit constraints on the possible frequency-response. One beneficial feature of this time-domain spline characterization is that it attenuates the impact of measurement noise in regions of the spectrum where the input PRN codes have low signal power. Thus, an important goal of the Weiner filter methods of Refs. 4 and 5 is achieved implicitly through this modeling choice.

A third difference from the methods of Refs. 4 and 5 is its choice of system identification measurement model. These two references use the frequency-domain version of the direct relationship between the input PRN code and the raw RF front-end samples. The present approach inserts a pre-processing step in order to develop an alternate "measurement" model. It computes the cross-

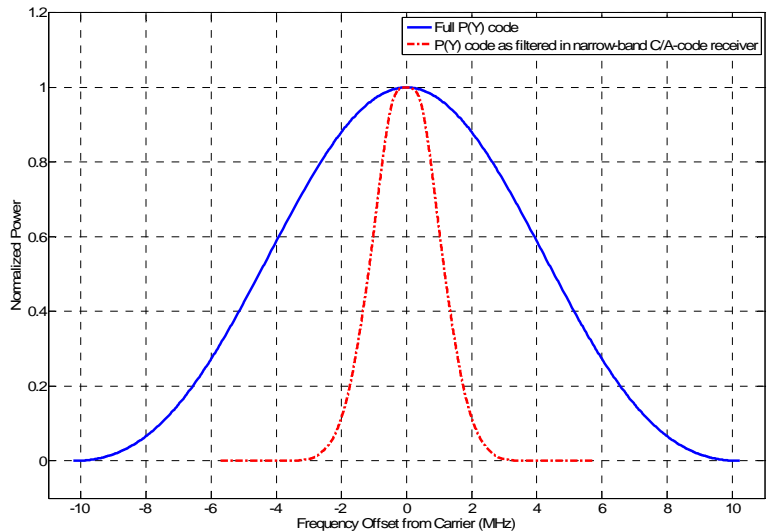


Fig. 1. The full main lobe of the P(Y) code power spectrum (solid blue) and its highly filtered spectrum at the output of an inexpensive narrow-band C/A-code RF front-end (dash-dotted red).

correlation between the received PRN code and the original wide-band PRN code, as is done in typical real-time receiver processing. It does this for many early and late offsets from the prompt tracked PRN code, and it averages its results over long data windows, over a minute or more. The calculations may involve hundreds of code delay offsets spread over an interval of 5 to 10 PRN chips. The system identification "measurement" model is the mathematical relationship between this "measured", distorted cross-correlation function and the convolution of the filter impulse response function with the original wide-band PRN code auto-correlation function. This type of model is more suitable for off-line calculations. It removes most of the effects of variable PRN code Doppler shift by using a DLL to track the prompt PRN code during the entire data window. A second benefit of this approach is that it can compress hundreds of millions of raw RF samples into a few hundred cross-correlation values prior to the application of least-squares system identification calculations. Direct system identification calculations using 5×10^8 raw RF samples would be impractical.

A fourth difference from Refs. 3, 4, 5, and 6 is that the present paper presents system identification results for actual live GPS data. These earlier works concentrate on proofs of concept using simulated data. Given that they had more ambitious goals, the characterization of entire transmission channels, it is reasonable that they relied on simulation because one can know "truth" in that case. With this paper's less ambitious goal of characterizing only the filter, less rigorous checks suffice, such as consistency between multiple channels and effectiveness in the P(Y) code semi-codeless processing calculations of Ref. 1.

This paper makes three contributions to modeling and system identification of an RF filter complex envelop impulse response function. First, it develops a time-domain model of the relationship between the impulse response function and PRN auto-correlation function on the one hand and the distorted cross-correlation of the PRN code with the received signal on the other hand. It also develops a practical recipe for computing "measured" values of the latter quantity at many code phases and averaged over long data batches.

The second contribution is the definition of a spline-based model of the RF filter impulse response function and the development of a system identification problem for its parameters. The resulting problem reduces to an over-determined linear least-squares problem in the unknown complex spline node parameters. An extension of this technique enables the simultaneous use of data from multiple GNSS signals from the same receiver in a single system identification calculation for a single filter impulse response function.

The third contribution is the application of this technique to actual GNSS data and an evaluation of its effectiveness. The data are from two distinct GPS C/A-code receiver designs that have RF front-ends with bandwidths on the order of 2 MHz. The method's effectiveness is demonstrated by its ability to accurately fit the cross-correlation distortions of multiple PRN codes using a single filter impulse response function. A second check compares the corresponding frequency responses to gain plots that are available from the filter manufacturers.

This paper consists of 5 main sections followed by conclusions. Section II presents mathematical models of the received signal, of its cross-correlation with the wide-band transmitted PRN code, and of the relationship between the wide-band autocorrelation function, the RF filter impulse response function, and the "measured" cross-correlation function. This section develops a recipe for computing a normalized "measured" cross-correlation function from measured RF data and DLL tracking results. Section III develops the spline model of the RF filter's complex envelop impulse response function. It uses this model in the cross-correlation relationship of Section II in order to develop an over-determined system of linear equations for the unknown spline coefficients. These are the basic system identification equations. Section IV generalizes the system identification problem of Section III in order to handle data from multiple PRNs simultaneously. It develops a technique for solving these equations, which are mostly linear but which contain small nonlinearities from possible differential delays between the different signals. Section V applies this paper's methods to real data and presents results. Its results are based on off-line MATLAB processing of stored RF front-end data. Section VI discusses open questions about these methods and suggests future studies that can address these concerns. Section VII summarizes the results and presents conclusions.

II. TIME-DOMAIN MODELS OF SIGNALS, FILTER RESPONSES, AND CROSS-CORRELATIONS

A. Modeling the Effect of the RF Filter on the Received Signal

Development of the system identification technique starts with a model of the received signal. This model uses the RF filter impulse response function in order to characterize the relationship of the original wide-band PRN code at the input of the RF front-end to the filtered PRN code at the output. It takes the form

$$y_i = AZ_f(t_i) \cos[\omega_{IF}t_i + \phi(t_i)] + v_i \quad (1)$$

where y_i is the output by the receiver's RF front-end at sample time t_i , A is the original signal amplitude, $Z_f(t)$ is the filtered version of the PRN code time history at the output of the RF front-end, ω_{IF} is the intermediate

frequency to which the RF carrier gets mixed by the RF front-end, $\phi(t)$ is the negative beat carrier phase, and v_i is the receiver noise. This noise is assumed to be white-noise with statistics:

$$E\{v_i\} = 0, E\{v_i^2\} = \sigma_{RF}^2, E\{v_i v_l\} = 0 \text{ for all } i \neq l \quad (2)$$

If $\Delta t = t_{i+1} - t_i$ is the RF sample interval, then the received carrier-to-noise ratio is $C/N_0 = A^2 \bar{Z}_f^2 / (4\sigma_{RF}^2 \Delta t)$, where \bar{Z}_f^2 is the average power of the filtered PRN code $Z_f(t)$. For a wide-band receiver and a BPSK PRN code, \bar{Z}_f^2 will equal 1. In a narrow-band receiver, it will be less than 1.

This part of the analysis ignores the possible presence of navigation data bits that modulate $Z_f(t)$. Subsection II.C discusses how this paper's methods deal sensibly with data bits if they are present in the signal.

The filtered PRN code time history depends on the corresponding wide-band time-history $Z(t)$ and on the RF front-end filter's envelop impulse response function $h(t)$. This dependence takes the form of a convolution integral:

$$\begin{aligned} Z_f(t) &= \int_{t-t_{max}}^t h(t-\tau)Z(\tau+\tau_D)d\tau \\ &= \int_{-\infty}^{\infty} h(t-\tau)Z(\tau+\tau_D)d\tau \end{aligned} \quad (3)$$

The quantity τ_D is the time delay between the arrival of a given PRN code chip of $Z(t)$ at the input to the RF front-end and the replay of that same code chip by the receiver DLL's prompt number-controlled oscillator. This delay is needed in Eq. (3) because all times are given as receiver clock times. The system identification calculation can trace to this time system all RF data and all $Z(t)$ replicas that it uses to compute cross-correlations, but it never knows exactly when the received PRN code arrived at the RF front-end input. Therefore, τ_D is never known exactly. An arbitrary choice of τ_D , provided that it is not too small, will suffice for purposes of this paper's system identification calculations. The particular estimate of the impulse response function $h(t)$ will, of course, depend on the choice of τ_D . Fortunately, it will be possible to use the chosen τ_D and the corresponding estimate of $h(t)$ in order to predict the distortion and delay of any other arbitrary signal measured with respect to receiver time in a way that is insensitive to the particular choice of τ_D .

Equation (3) models $h(t)$ as being a finite impulse response of duration t_{max} . That is, it presumes that $h(t) = 0$ for all $t > t_{max}$. This represents an approximation that is inexact due to the analog nature of the RF front-end filters. This approximation is needed in order to develop a spline model of $h(t)$ for use in the system identification problem modeling of Section III. This approximation will not cause any significant loss of fidelity if t_{max} is chosen to be large enough. Of course, Eq. (3) also

assumes that $h(t) = 0$ for all $t < 0$. This assumption preserves causality.

The extension of the limits of integration on the extreme-right-hand side of Eq. (3) is useful for later analysis. It is consistent with the assumption that $h(t) = 0$ for all $t < 0$ and for all $t > t_{max}$.

The impulse response model in Eq. (3) assumes that all channel distortion occurs in the RF front-end filter. In reality, distortion also arises due to the transmitter's filter and due to multi-path. This paper's technique will identify the full channel response, not just that of the receiver's RF filtering. The target application of these techniques is for identification of impulse response functions for narrow-band filters in inexpensive GPS C/A-code RF front-ends. Their bandwidths are typically on the order of 2 to 3 MHz because the main lobe of the C/A code is only 2.046 MHz wide. Therefore, distortion at the transmitter, whose filter bandwidth is at least 20.46 MHz, will be negligible relative to the distortion caused by the receiver's filter. The isolation of receiver filter effects from multi-path effects is more problematic. As discussed below, the use of multiple PRN signals for simultaneous system identification should help to mitigate any multi-path influence on the resulting $h(t)$ estimate.

The wide-band $Z(t)$ PRN code used in Eq. (3) could be any GNSS signal. It could be C/A code, P(Y) code, an L5 code, or a Galileo code. The only requirement from the standpoint of the present analyses is that it be a known code. Thus, one would need knowledge of the P(Y) code, likely only on an after-the-fact bases, in order to carry out this paper's system identification calculations based on that signal. C/A code is used in the example applications of Section V.

The filtered, distorted $Z_f(t)$ signal and the filter impulse response $h(t)$ are both modeled as being complex base-band signals. This approach enables the system identification calculation to include the possibility of asymmetry in the filter's frequency response

B. Impulse Relationship between Filtered and Wide-Band Correlation Functions

The receiver has the capacity to compute the cross-correlation between a replica of the wide-band PRN code $Z(t)$ and the received, filtered version $Z_f(t)$. An analytical model of this cross-correlation function takes the form:

$$C_{Z_f Z}(\eta) = \lim_{T \rightarrow \infty} \frac{1}{2T} \int_{-T}^T Z_f(t)Z(t-\eta)dt \quad (4)$$

One can substitute the $Z_f(t)$ model from Eq. (3) into Eq. (4) in order to derive a relationship between this filtered cross-correlation function and the known wide-band autocorrelation function of $Z(t)$. The latter function is

$$C_{ZZ}(\eta) = \lim_{T \rightarrow \infty} \frac{1}{2T} \int_{-T}^T Z(t)Z(t-\eta)dt \quad (5)$$

The derivation of the desired formula goes as follows:

$$\begin{aligned}
C_{ZfZ}(\eta) &= \lim_{T \rightarrow \infty} \frac{1}{2T} \int_{-T}^T \left[\int_{-\infty}^{\infty} h(t-\tau)Z(\tau+\tau_D)d\tau \right] Z(t-\eta)dt \\
&= \lim_{T \rightarrow \infty} \frac{1}{2T} \int_{-T}^T \left[\int_{-\infty}^{\infty} h(\xi)Z(t-\xi+\tau_D)d\xi \right] Z(t-\eta)dt \\
&= \int_{-\infty}^{\infty} h(\xi) \left[\lim_{T \rightarrow \infty} \frac{1}{2T} \int_{-T}^T Z(t-\xi+\tau_D)Z(t-\eta)dt \right] d\xi \\
&= \int_{-\infty}^{\infty} h(\xi) \left[\lim_{T \rightarrow \infty} \frac{1}{2T} \int_{-T-\eta}^{T-\eta} Z(\gamma+\eta-\xi+\tau_D)Z(\gamma)d\gamma \right] d\xi \\
&= \int_{-\infty}^{\infty} h(\xi)C_{ZZ}(\xi-\eta-\tau_D)d\xi \\
&= \int_0^{t_{max}} h(t)C_{ZZ}(t-\eta-\tau_D)dt \\
&= \int_{\eta+\tau_D-t_{max}}^{\eta+\tau_D} h(\eta+\tau_D-\tau)C_{ZZ}(\tau)d\tau \tag{6}
\end{aligned}$$

The second line of the above derivation follows from the first by changing the dummy inner integration variable from τ to $\xi = t - \tau$. The third line changes the order of integration from that of the second line and moves the T limiting calculation within the outside integral. These are allowable operations for the signals of interest. The fourth line changes the dummy inner integration variable from t to $\gamma = t - \eta$. The fifth line replaces the bracketed expression in the fourth line with $C_{ZZ}(\eta - \xi + \tau_D)$. A careful comparison of this bracketed expression with Eq. (5) demonstrates the desired equivalence if one recognizes that the result in Eq. (5) is independent of any possible bias in its limits of integration, such as appears in the bracketed expression on the fourth line of Eq. (6). The sixth line of Eq. (6) is derived from the fifth line by changing the name of the dummy integration variable from ξ to t and by recalling that $h(t) = 0$ for $t < 0$ and for $t > t_{max}$. The seventh line is derived from the sixth line by changing the dummy integration variable from t to $\tau = -t + \eta + \tau_D$ while exploiting the evenness of $C_{ZZ}(\eta)$.

The last line of Eq. (6) demonstrates that $C_{ZfZ}(\eta)$ is related to $C_{ZZ}(\eta)$ via a convolution with $h(t)$. This relationship is similar to the relationship of the filtered PRN code $Z_f(t)$ to its wide-band counterpart $Z(t)$, as per Eq. (3).

The most important result of Eq. (6) is its sixth line. This is the relationship that will be exploited for system identification purposes. In order to emphasize this fact, the result is repeated below as a distinct equation:

$$C_{ZfZ}(\eta) = \int_0^{t_{max}} h(t)C_{ZZ}(t-\eta-\tau_D)dt \tag{7}$$

The strategy for using Eq. (7) to perform system

identification rests on having a priori knowledge of $C_{ZZ}(\eta)$ and on an ability to "measure" a scaled version of $C_{ZfZ}(\eta)$. Given multiple "measurements" of $C_{ZfZ}(\eta_m)$ at multiple code delay offsets, η_m for $m = 1, \dots, M$, an over-determined system of M equations can be developed. These equations can be used in order to estimate parameters that characterize $h(t)$ by solving a least-squares problem.

Up to this point, scare quotes have been used to designate the "measurement" $C_{ZfZ}(\eta_m)$. These quotes indicate that $C_{ZfZ}(\eta_m)$ is not a raw measurement. Rather, it is a quantity that is derived from raw RF front-samples via extensive signal processing calculations. These calculations are the subject of this paper's next subsection. In the interests of simplicity, the scare quotes will be dropped from now on with the understanding that terms such as "measure" and "measured" are used in a loose sense to signify that $C_{ZfZ}(\eta_m)$ has been derived based on measured data.

C. Processing of Receiver Data to Measure the Filtered/Wide-Band PRN Code Cross-Correlation Function

The system identification method relies on the ability of a GPS receiver to measure the value of $C_{ZfZ}(\eta)$. This must be done at a number of values of the wide-band replica code's time offset from the prompt code, η . The signal amplitude A from Eq. (1) is not known a priori. Therefore, it is necessary to compute a normalized measurement that has an unknown scaling relative to the desired measurement $C_{ZfZ}(\eta)$. Suppose that this normalized version is called $\tilde{C}_{ZfZ}(\eta)$. It is related to the cross-correlation as follows:

$$C_{ZfZ}(\eta) = A_c \tilde{C}_{ZfZ}(\eta) \tag{8}$$

where A_c is an unknown constant scaling factor. This factor will be estimated as part of the system identification process.

The choice of scaling for $\tilde{C}_{ZfZ}(\eta)$ and the associated value of A_c are somewhat arbitrary, subject to the constraint that they be consistent. A convenient scaling is to define these quantities so that $\tilde{C}_{ZfZ}(0) = 1$ identically. In this case, the complex value of A_c characterizes the correlation amplitude loss of the prompt code and any phase rotation that it may undergo. That is, $C_{ZfZ}(0) = A_c$. It is normally a value in the neighborhood of 1. It approaches 1 as the RF filter distortion approaches zero.

The computation of $\tilde{C}_{ZfZ}(\eta)$ is carried out using receiver RF front-end samples. The initial part of this calculation is a set of standard correlation accumulation operations that rely on the results of DLL tracking of the PRN code phase and PLL tracking of the carrier phase. The needed

in-phase and quadrature accumulations are

$$I_k(\eta) = \sum_{i=i_k}^{i_k+N_k-1} y_i Z_{nom}[(t_i - \tau_k - \eta)(1 + \hat{\omega}_{Dk}/\omega_c)] \times \cos[\omega_{IF}t_i + \hat{\phi}_k + \hat{\omega}_{Dk}(t_i - \tau_k)] \quad (9a)$$

$$Q_k(\eta) = \sum_{i=i_k}^{i_k+N_k-1} y_i Z_{nom}[(t_i - \tau_k - \eta)(1 + \hat{\omega}_{Dk}/\omega_c)] \times \sin[\omega_{IF}t_i + \hat{\phi}_k + \hat{\omega}_{Dk}(t_i - \tau_k)] \quad (9b)$$

for the k^{th} accumulation interval, which starts at receiver time τ_k and ends at τ_{k+1} . The Doppler-shifted wide-band PRN code is replica $Z(t) = Z_{nom}[t(1 + \hat{\omega}_{Dk}/\omega_c)]$, where $Z_{nom}(t)$ is the known nominal PRN code with no code Doppler shift, $\hat{\omega}_{Dk}$ is the PLL's carrier Doppler shift estimate for this interval, and ω_c is the nominal broadcast carrier frequency. The two times τ_k and τ_{k+1} must be chosen by the DLL, and $Z(t)$ must be synchronized by the DLL so that $Z(t - \tau_k)$ is the prompt PRN code replica during this interval. The sample index i_k is the first sample such that $\tau_k \leq t_i$. The quantity N_k is the total number of samples in the interval so that the terminal index i_k+N_k-1 is the largest value of i such that $t_i < \tau_{k+1}$. The phase $\hat{\phi}_k$ is the estimated negative beat carrier phase at the start time τ_k .

The accumulations in Eqs. (9a) and (9b) are unnormalized. An initial rough normalization is carried out on a per-accumulation basis using the following operations:

$$\tilde{I}_k(\eta) = I_k(\eta)I_k(0) + Q_k(\eta)Q_k(0) - 2\sigma_{IQ}^2 C_{ZZ}(\eta) \quad (10a)$$

$$\tilde{Q}_k(\eta) = -I_k(\eta)Q_k(0) + Q_k(\eta)I_k(0) \quad (10b)$$

$$\tilde{I}_k(0) = \tilde{I}_k(\eta) / \tilde{I}_k(0) \quad (10c)$$

$$\tilde{Q}_k(0) = \tilde{Q}_k(\eta) / \tilde{I}_k(0) \quad (10d)$$

where σ_{IQ} in Eq. (10a) is the standard deviation of the receiver noise effects on $I_k(\eta)$ and $Q_k(\eta)$. This is assumed to be constant and independent of the offset η . It can be estimated from accumulation data using standard techniques, e.g., see Eqs.(23a)-(24b) of Ref. 1. The subtraction term on the extreme right-hand side of Eq. (10a) acts to remove the principal bias caused by noise-correlations between $I_k(0)$ and $I_k(\eta)$ and between $Q_k(0)$ and $Q_k(\eta)$.

At this point in the calculations, $\tilde{I}_k(0) = 1$ and $\tilde{Q}_k(0) = 0$ are guaranteed. In addition to normalizing $\tilde{I}_k(0)$, these computations remove any effects of navigation data bits. Thus, there is no need to consider their effects anywhere in the remainder of this paper.

One might be tempted simply to average the values of $\tilde{I}_k(\eta)$ and $\tilde{Q}_k(\eta)$ over many accumulation intervals in

order to determine, respectively, the real and imaginary parts of $\tilde{C}_{ZZ}(\eta)$. Unfortunately, there would be a residual bias in the resulting $\tilde{C}_{ZZ}(\eta)$ value due to the impact on the operations in Eqs. (10c) and (10d) of correlations of the measurement noise effects in $\tilde{I}_k(0)$ with those in $\tilde{I}_k(\eta)$ and $\tilde{Q}_k(\eta)$. These biases are removed in the following calculation of $\tilde{C}_{ZZ}(\eta)$

$$\tilde{C}_{ZZ}(\eta) = \frac{\frac{1}{K} \sum_{k=1}^K \tilde{I}_k(\eta) + C_{ZZ}(\eta)\mu}{1 + \mu} + \sqrt{-1} \left[\frac{1}{K} \sum_{k=1}^K \tilde{Q}_k(\eta) \right] \frac{1}{1 + \zeta} \quad (11)$$

where K is the total number of accumulations used to form $\tilde{C}_{ZZ}(\eta)$. The small correction quantities ζ and μ are functions of the accumulations' signal-to-noise ratio, which equals the carrier-to-noise ratio multiplied by the average accumulation interval. They take on the values:

$$\zeta = \frac{1}{(C/N_0)\bar{T}_{accum}} \quad (12a)$$

$$\mu = \zeta(1 + \zeta) \quad (12b)$$

where

$$\bar{T}_{accum} = \frac{\Delta t}{K} \sum_{k=1}^K N_k \quad (13)$$

is the average length of an accumulation interval. The correction terms to the in-phase and quadrature averages in Eq. (11) are small for a sufficiently high carrier-to-noise ratio and a sufficiently long accumulation interval. The carrier-to-noise ratio of the signal used in Eq. (12a) can be estimated from the accumulations using standard techniques, e.g., using Eqs. (23a)-(26) of Ref. 1.

The derivation of Eq. (11) presumes that the wide-band autocorrelation function is normalized, i.e., that $C_{ZZ}(0) = 1$. This same assumption also applies to Eq. (10a). Therefore, the calculations in Eqs. (10a)-(11) enforce the normalization $\tilde{C}_{ZZ}(0) = 1$ regardless of the magnitudes of ζ and μ .

Formulation of the system identification problem requires that computations in Eqs. (9a)-(11) be repeated M times, once for each distinct PRN code phase offset η_m for $m = 1, \dots, M$. Typically M on the order of 300 offsets might be used. The values of η_m might range from -5 code chips to +5 code chips. Recall that negative η_m values correspond to early code replicas in the Eqs. (9a) and (9b) accumulation calculations. Positive values correspond to late replicas.

III. SYSTEM IDENTIFICATION OF A SPLINE MODEL OF THE IMPULSE RESPONSE

Given the model in Eqs. (7) and (8) and the measurements that are synthesized using Eqs. (9a)-(11), it is possible to formulate a linear system of equations that form the bases of determining the $h(t)$ impulse response function. As a first step in developing a feasible computation procedure, the infinite-dimensional unknown $h(t)$ function must be represented approximately by a finite set of parameters. Afterwards, the system identification problem can be formulated in terms of those parameters.

A. Spline Model of $h(t)$

The choice of a finite-dimensional representation of $h(t)$ is somewhat arbitrary. The form used here is that of the first derivative of a quintic spline. A quintic spline can be represented by its function values and their first and second derivatives at a set of spline node points. It is continuous with continuous first and second derivatives. The quintic spline, being the integral of the impulse response, is the envelop filter's step response.

The derivative-of-a-quintic-spline modeling approach simplifies enforcement of the following unit normalization constraint:

$$\int_0^{t_{max}} h(t) d\tau = 1 \quad (14)$$

Enforcement is achieved automatically by requiring that the corresponding step response be a unit step response. This constraint is needed in order to preserve simultaneous observability of the spline parameters and the cross-correlation scaling parameter A_c . Without such a constraint, the value of A_c and of the spline node parameters could be increased by any arbitrary common factor without affecting the relative accuracy with which the measurement model in Eq. (7) was satisfied. The choice of unit normalization of $h(t)$ is equivalent to normalizing the frequency-response model of the filter to have a gain of 0 dB at its center frequency. Thus, it is a reasonable choice.

The spline-based parametric model of $h(t)$ takes the form:

$$h(t; \mathbf{p}) = \left. \frac{dg}{dt} \right|_{(t; \mathbf{p})} \quad (15)$$

where $g(t; \mathbf{p})$ is the filter's unit impulse response function. The spline is defined using L_s+1 equal-length quintic intervals that cover the range from $t = 0$ to $t = t_{max}$. The spline node points at the ends of these intervals are $t_{sl} = l\Delta t_s$ for $l = 0, \dots, (L_s+1)$ where $\Delta t_s = t_{max}/(L_s+1)$. The elements of \mathbf{p} are the values of g and its first and second time derivatives at the internal spline node points t_{sl} for $l = 1, \dots, L_s$. The $g(t; \mathbf{p})$ values at the end nodes of the

spline are pre-defined to enforce smoothness and the unit normalization: $g(0; \mathbf{p}) = 0$, $g(t_{max}; \mathbf{p}) = 1$, and the first and second time derivatives of $g(t; \mathbf{p})$ are zero at both $t = 0$ and $t = t_{max}$. These definitions translate into the following spline parameter vector definition:

$$\mathbf{p} = \begin{bmatrix} g_1 \\ g_2 \\ \vdots \\ g_{L_s} \\ h_1 \\ h_2 \\ \vdots \\ h_{L_s} \\ \dot{h}_1 \\ \dot{h}_2 \\ \vdots \\ \dot{h}_{L_s} \end{bmatrix} \quad (16)$$

where the parameters g_l , h_l , and \dot{h}_l are, respectively, the values $g(t)$, $h(t)$, and dh/dt evaluated at the spline node point t_{sl} for $l = 1, \dots, L_s$. The full spline definition uses an extension of this parameter set to include the pre-defined end node values $g_0 = 0$, $h_0 = 0$, $\dot{h}_0 = 0$ at $t_{s0} = 0$ and $g_{(L_s+1)} = 1$, $h_{(L_s+1)} = 0$, and $\dot{h}_{(L_s+1)} = 0$ at $t_{s(L_s+1)} = t_{max}$. The splined $h(t; \mathbf{p})$ function can be defined in terms of the derivative of a generic quintic spline derivative function that is defined over an interval of unit length. This generic spline derivative function is

$$\begin{aligned} \hat{h}(\tau; g_0, g_1, \dot{h}_0, \dot{h}_1, \ddot{h}_0, \ddot{h}_1) = & \\ & (g_1 - g_0)(30\tau^2 - 60\tau^3 + 30\tau^4) \\ & + \dot{h}_0(1 - 18\tau^2 + 32\tau^3 - 15\tau^4) \\ & + \dot{h}_1(-12\tau^2 + 28\tau^3 - 15\tau^4) \\ & + \ddot{h}_0(\tau - 4.5\tau^2 + 6\tau^3 - 2.5\tau^4) \\ & + \ddot{h}_1(1.5\tau^2 - 4\tau^3 + 2.5\tau^4) \end{aligned} \quad (17)$$

Using this function, the definition of the impulse response becomes:

$$h(t; \mathbf{p}) = \begin{cases} 0 & \text{if } t < 0 \\ \hat{h}\left[\frac{t-t_{sl}}{\Delta t_s}; \frac{g_l}{\Delta t_s}, \frac{g_{l+1}}{\Delta t_s}, h_l, \right. \\ \quad \left. h_{l+1}, \Delta t_s \dot{h}_l, \Delta t_s \dot{h}_{l+1}\right] & \text{if } t_{sl} \leq t < t_{sl+1} \\ 0 & \text{if } t_{max} \leq t \end{cases} \quad (18)$$

where the middle condition in Eq. (18) is valid for all spline indices l in the range 0 to L_s .

Figure 2 plots example $g(t; \mathbf{p})$ and $h(t; \mathbf{p})$ functions for a

spline with $L_s+1 = 5$ quintic intervals that span from 0 to $t_{max} = 5 \mu\text{sec}$. The top graph plots the real and imaginary parts of $g(t;\mathbf{p})$ as, respectively, dash-dotted blue and green curves. The bottom graph plots the real and imaginary parts $h(t;\mathbf{p})$ as, respectively, solid blue and green curves. The parameter vector \mathbf{p} has $3L_s = 12$ elements in this case. The real and imaginary parts of the first 4 elements of \mathbf{p} are the spline node values shown on the upper $g(t;\mathbf{p})$ plot at the points $t = 1, 2, 3,$ and $4 \mu\text{sec}$ as, respectively, the red squares and the brown diamonds. Similarly, the real and imaginary parts of elements 5 through 8 of \mathbf{p} are the spline node values shown on the lower $h(t;\mathbf{p})$ plot at the same 4 time points and using the same symbol definitions. The values of elements 9 through 12 of \mathbf{p} are not directly plotted on Fig. 2. Their real and imaginary parts constitute the slopes of the lower $h(t;\mathbf{p})$ real and imaginary plots at the 4 node points.

The system identification calculation needs to be able to compute the partial derivatives of $h(t;\mathbf{p})$ with respect to the elements of \mathbf{p} . These can be characterized in terms of the six partial derivatives of the generic quintic spline derivative function in Eq. (17) with respect to its parameters. These are

$$\left. \frac{\partial \hat{h}}{\partial g_0} \right|_{\tau} = -30\tau^2 + 60\tau^3 - 30\tau^4 \quad (19a)$$

$$\left. \frac{\partial \hat{h}}{\partial g_1} \right|_{\tau} = 30\tau^2 - 60\tau^3 + 30\tau^4 \quad (19b)$$

$$\left. \frac{\partial \hat{h}}{\partial h_0} \right|_{\tau} = 1 - 18\tau^2 + 32\tau^3 - 15\tau^4 \quad (19c)$$

$$\left. \frac{\partial \hat{h}}{\partial h_1} \right|_{\tau} = -12\tau^2 + 28\tau^3 - 15\tau^4 \quad (19d)$$

$$\left. \frac{\partial \hat{h}}{\partial \dot{h}_0} \right|_{\tau} = \tau - 4.5\tau^2 + 6\tau^3 - 2.5\tau^4 \quad (19e)$$

$$\left. \frac{\partial \hat{h}}{\partial \dot{h}_1} \right|_{\tau} = 1.5\tau^2 - 4\tau^3 + 2.5\tau^4 \quad (19f)$$

Using these functions, the parameter partial derivatives of $h(t;\mathbf{p})$ are

$$\left. \frac{\partial h}{\partial g_l} \right|_t = \begin{cases} 0 & \text{if } t < t_{sl-1} \\ \frac{1}{\Delta t_s} \left. \frac{\partial \hat{h}}{\partial g_1} \right|_{[(t-t_{sl-1})/\Delta t_s]} & \text{if } t_{sl-1} \leq t < t_{sl} \\ \frac{1}{\Delta t_s} \left. \frac{\partial \hat{h}}{\partial g_0} \right|_{[(t-t_{sl})/\Delta t_s]} & \text{if } t_{sl} \leq t < t_{sl+1} \\ 0 & \text{if } t_{sl+1} \leq t \end{cases} \quad (20a)$$

$$\left. \frac{\partial h}{\partial h_l} \right|_t = \begin{cases} 0 & \text{if } t < t_{sl-1} \\ \left. \frac{\partial \hat{h}}{\partial h_1} \right|_{[(t-t_{sl-1})/\Delta t_s]} & \text{if } t_{sl-1} \leq t < t_{sl} \\ \left. \frac{\partial \hat{h}}{\partial h_0} \right|_{[(t-t_{sl})/\Delta t_s]} & \text{if } t_{sl} \leq t < t_{sl+1} \\ 0 & \text{if } t_{sl+1} \leq t \end{cases} \quad (20b)$$

$$\left. \frac{\partial h}{\partial \dot{h}_l} \right|_t = \begin{cases} 0 & \text{if } t < t_{sl-1} \\ \Delta t_s \left. \frac{\partial \hat{h}}{\partial \dot{h}_1} \right|_{[(t-t_{sl-1})/\Delta t_s]} & \text{if } t_{sl-1} \leq t < t_{sl} \\ \Delta t_s \left. \frac{\partial \hat{h}}{\partial \dot{h}_0} \right|_{[(t-t_{sl})/\Delta t_s]} & \text{if } t_{sl} \leq t < t_{sl+1} \\ 0 & \text{if } t_{sl+1} \leq t \end{cases} \quad (20c)$$

where Eqs. (20a)-(20c) are valid for all spline parameter indices l in the range 1 to L_s .

An important property of these partial derivative functions is that none of them depends on any of the parameter values in \mathbf{p} . This property arises from the linear dependence of $h(t;\mathbf{p})$ on \mathbf{p} as dictated by the model definition in Eqs. (17) and (18). The linearity of the dependence on the values in \mathbf{p} causes the underlying parameter identification problem to be linear, which is a great advantage in terms of ease of solution. Because of this linearity, it is possible to express $h(t;\mathbf{p})$ in the linear form

$$h(t;\mathbf{p}) = h(t;0) + \left. \frac{\partial h}{\partial \mathbf{p}} \right|_t \mathbf{p} \quad (21)$$

where the needed partial derivative row vector is

$$\left. \frac{\partial h}{\partial \mathbf{p}} \right|_t = \left[\left. \frac{\partial h}{\partial g_1} \right|_t, \left. \frac{\partial h}{\partial g_2} \right|_t, \dots, \left. \frac{\partial h}{\partial g_{L_s}} \right|_t, \left. \frac{\partial h}{\partial h_1} \right|_t, \left. \frac{\partial h}{\partial h_2} \right|_t, \dots, \left. \frac{\partial h}{\partial h_{L_s}} \right|_t, \left. \frac{\partial h}{\partial \dot{h}_1} \right|_t, \left. \frac{\partial h}{\partial \dot{h}_2} \right|_t, \dots, \left. \frac{\partial h}{\partial \dot{h}_{L_s}} \right|_t \right] \quad (22)$$

As stated in the introduction, an important property of this spline model is that it can help to smooth out the effects of measurement noise on the estimate of $h(t;\mathbf{p})$. This occurs because the number of parameters used to model $h(t;\mathbf{p})$, which equals $3L_s$, i.e. three times the number of non-end-point spline nodes, is normally small compared to the number of data points. Therefore, the estimate of each parameter effectively averages the information of many measurements. This is in stark contrast with the spectral estimation methods of Refs. 4 and 5. Those methods effectively use a large number of parameters to represent $h(t)$: all of the complex phasors of an FFT of $h(t)$ on a dense grid of frequency points. This large number of parameters has the effect of passing

much of the measurement noise through to the resulting $h(t)$, making it much less smooth and likely more noisy.

Of course, this advantage of the present method comes with a risk. If the parameterization of $h(t;\mathbf{p})$ does not provide for a sufficient richness of possible impulse time histories, then it may be impossible to accurately represent the true $h(t)$ in this manner, and the accuracy of $h(t;\mathbf{p})$ will be poor. Therefore, the practitioner must make a trade-off: One must make L_s large enough to allow $h(t;\mathbf{p})$ to approximate the true impulse response accurately, but one must not make L_s too large; otherwise the resulting $h(t;\mathbf{p})$ will use its extra degrees of freedom primarily to fit measurement noise that is not representative of the true impulse response.

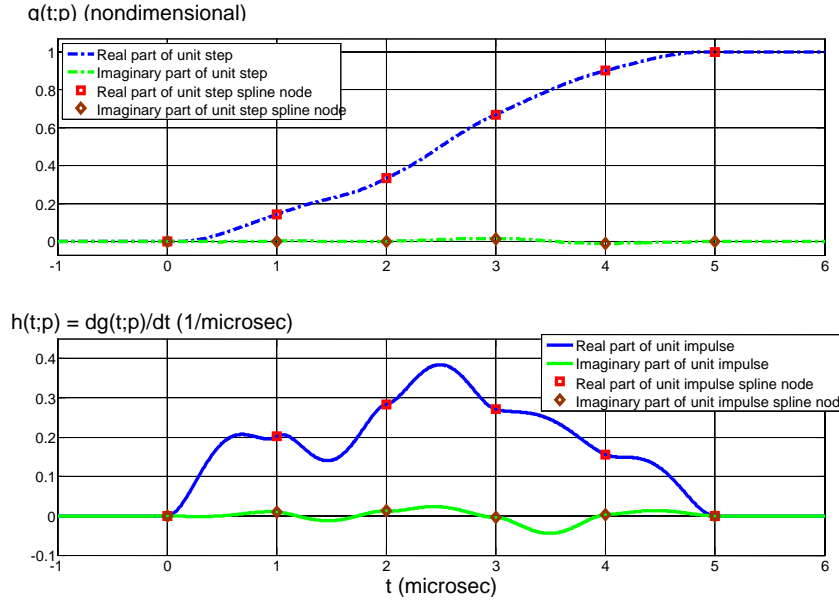


Fig. 2. Example quintic-splined $g(t;\mathbf{p})$ unit step response (top plot) and the corresponding $h(t;\mathbf{p})$ unit impulse response (bottom plot).

B. Linear Parameter Identification Problem for the Spline Node Values and the Scaling Factor

The spline-based model of $h(t;\mathbf{p})$ from the previous subsection can be combined with the cross-correlation model in Eq. (7) and the re-normalization correlation measurement model in Eq. (8) to develop a system of equations for the unknown elements of the vector $[\mathbf{p}; A_c]$. Using the linear form of the spline impulse response model in Eq. (21), the resulting equations take the form:

$$A_c \tilde{C}_{ZZ}(\eta_m) = \int_0^{t_{max}} h(t;0) C_{ZZ}(t - \eta_m - \tau_D) dt + \left[\int_0^{t_{max}} \frac{\partial h}{\partial \mathbf{p}} \Big|_t C_{ZZ}(t - \eta_m - \tau_D) dt \right] \mathbf{p} \quad (23)$$

for $m = 1, \dots, M$

These equations can be formed into a standard over-

determined matrix-vector linear system of equations. In order to do this, define the following row vectors and scalars:

$$\partial \mathbf{c}_m^T = \left[\int_0^{t_{max}} \frac{\partial h}{\partial \mathbf{p}} \Big|_t C_{ZZ}(t - \eta_m - \tau_D) dt \right] \quad (24a)$$

for $m = 1, \dots, M$

$$c_{0m} = \int_0^{t_{max}} h(t;0) C_{ZZ}(t - \eta_m - \tau_D) dt \quad (24b)$$

for $m = 1, \dots, M$

The row vector $\partial \mathbf{c}_m^T$ has $3L_s$ elements, the same number as in the column vector \mathbf{p} .

The integrals in Eqs. (24a) and (24b) can be evaluated exactly for typical PRN codes. This is true because the known wide-band PRN code autocorrelation function $C_{ZZ}(t)$ is typically piecewise linear in t , while the nominal impulse response function $h(t;0)$ and its vector of partial derivative functions $\partial h / \partial \mathbf{p} \Big|_t$ are both piecewise quartic. Therefore, each integrand is piecewise quintic, and it can be integrated exactly by performing polynomial integration over each of its quintic intervals. Note that the individual intervals of piecewise quinticity may be smaller than the intervals of piecewise linearity of $C_{ZZ}(t)$ and the intervals of piecewise quarticity of $h(t;0)$ and $\partial h / \partial \mathbf{p} \Big|_t$. This happens because the intervals over which $C_{ZZ}(t)$ is linear are not necessarily the same intervals as those over which $h(t;0)$ and $\partial h / \partial \mathbf{p} \Big|_t$ are quartic. It is not very difficult to determine the proper intervals for performing each polynomial sub-integral. The ability to evaluate these integrals exactly is a significant benefit of having chosen a spline-based parametric model for $h(t)$.

Given the definitions in Eqs. (24a) and (24b), the M instances of Eq. (23) can be lumped into the following over-determined system of equations:

$$\begin{bmatrix} \tilde{C}_{ZZ}(\eta_1) \\ \tilde{C}_{ZZ}(\eta_2) \\ \tilde{C}_{ZZ}(\eta_3) \\ \vdots \\ \tilde{C}_{ZZ}(\eta_M) \end{bmatrix} A_c = \begin{bmatrix} c_{01} \\ c_{02} \\ c_{03} \\ \vdots \\ c_{0M} \end{bmatrix} + \begin{bmatrix} \partial \mathbf{c}_1^T \\ \partial \mathbf{c}_2^T \\ \partial \mathbf{c}_3^T \\ \vdots \\ \partial \mathbf{c}_M^T \end{bmatrix} \mathbf{p} \quad (25)$$

This problem can be recast into the following form

$$\tilde{\mathbf{c}}_{meas} A_c = \mathbf{c}_0 + H\mathbf{p} \quad (26)$$

if one defines the M -dimensional column vectors

$$\tilde{\mathbf{c}}_{meas} = \begin{bmatrix} \tilde{C}_{ZfZ}(\eta_1) \\ \tilde{C}_{ZfZ}(\eta_2) \\ \tilde{C}_{ZfZ}(\eta_3) \\ \vdots \\ \tilde{C}_{ZfZ}(\eta_M) \end{bmatrix} \quad (27a)$$

$$\mathbf{c}_0 = \begin{bmatrix} c_{01} \\ c_{02} \\ c_{03} \\ \vdots \\ c_{0M} \end{bmatrix} \quad (27b)$$

and the M -by- $(3L_s)$ -dimensional matrix

$$H = \begin{bmatrix} \partial \mathbf{c}_1^T \\ \partial \mathbf{c}_2^T \\ \partial \mathbf{c}_3^T \\ \vdots \\ \partial \mathbf{c}_M^T \end{bmatrix} \quad (28)$$

Equation (26) can be re-cast into the following standard linear least-squares form

$$-\mathbf{c}_0 = [H, -\tilde{\mathbf{c}}_{meas}] \begin{bmatrix} \mathbf{p} \\ A_c \end{bmatrix} \quad (29)$$

This equation is the principle system parameter identification equation of this paper. The M -dimensional column vector on its left-hand side is known as is the M -by- $(3L_s+1)$ matrix on its right-hand side. The unknown vector $[\mathbf{p}; A_c]$ on the right-hand side has $3L_s+1$ elements. If $M \geq (3L_s+1)$ and if the matrix on the right-hand side has linearly independent columns, then the parameters are observable, and the vector $[\mathbf{p}; A_c]$ can be determined using standard matrix techniques for solving over-determined linear least squares problems, techniques such as QR factorization⁷.

The lower limit on M requires that the number of PRN code timing offsets used to generate $\tilde{C}_{ZfZ}(\eta_m)$ measurements be no less than thrice the number of spine intervals less 2. Thus, one must be careful to calculate a sufficient number of independent $\tilde{C}_{ZfZ}(\eta_m)$ correlations for a given number of spline elements in the $h(t; \mathbf{p})$ model.

The measurements $\tilde{C}_{ZfZ}(\eta_m)$ for $m = 1, \dots, M$ appear in the final column of the matrix on the right-hand side of Eq. (29). This represents a somewhat unusual situation from a least-squares estimation standpoint. Normally the

measurements would enter the problem linearly as part of the known vector on the left-hand side of the equation. They enter the matrix in this case because of the need to estimate the re-scaling factor A_c that is introduced in Eq. (8). This fact has interesting consequences for the issue of how the measurement noise affects the solution accuracy. This question has been left for investigation at a later date.

One must be careful to solve this least-squares problem using linear algebra routines that are able to deal properly with complex numbers. Complex numbers arise in the problem because the measured correlations $\tilde{C}_{ZfZ}(\eta_m)$ can be complex. As a result, the optimal estimates of \mathbf{p} and A_c will be complex-valued.

One would expect A_c to be nearly real and somewhat near 1 for a filter that passes most of the $Z(t)$ PRN code. Therefore, the actual estimated value of A_c can give an indication of whether the problem and its solution make physical sense.

IV. SYSTEM IDENTIFICATION WITH SIMULTANEOUS PROCESSING OF DATA FOR MULTIPLE SIGNALS

The system identification problem in Eq. (29) can be generalized to handle multiple signals for multiple PRN codes simultaneously. The basic idea is to solve several versions of Eq. (29) simultaneously, one for each PRN for which $\tilde{C}_{ZfZ}(\eta_m)$ correlation measurements are available. Of course, these measurements must come from the same receiver and ideally from the same data span. They differ in their underlying PRN codes, in their cross-correlation measurements, and in their code Doppler shifts.

This multi-signal approach has several advantages. First, it probes the filter with additional data. It is always better to have more data in any estimation problem if there is a suitable model for the additional data. Second, the additional signals are likely to have different multi-path errors from each other. Given that the estimated $h(t)$ will include any multi-path effects, the simultaneous use of multiple signals provides a strategy for trying to attenuate the multi-path effects by averaging them over a number of signals.

A third advantage of using multiple signals is that any resultant diversity of their code Doppler shifts should enhance the problem observability. Recall from the introduction that Refs. 4 and 5 took pains to compensate for the fact that PRN codes have power nulls which cause their FFT-based filter models to have poor frequency response accuracy in the portions of the spectrum near these nulls. Although the present spline-based time-domain model has no direct analog of this problem, it is

believed that its frequency-domain equivalent may suffer some ill effects in these same low-power portions of the spectrum. Code Doppler shift diversity will place the nulls of different PRN codes in slightly different parts of the spectrum. This will enhance estimation accuracy because there will not be any portion of the spectrum where there is zero power to probe the filter response.

A. Independent Equations for Each Signal

The combined estimation problem with multiple signals is based on multiple independent versions of Eq. (29), one for each signal. Suppose that there are N signals. Then the multiple equations are

$$-\mathbf{c}_0^n(\tau_D^n) = [H^n(\tau_D^n), -\tilde{\mathbf{c}}_{meas}^n] \begin{bmatrix} \mathbf{p} \\ A_c^n \end{bmatrix} \text{ for } n = 1, \dots, N \quad (30)$$

where the superscript $(^n)$ indicates the signal number, not the quantity in question raised to the n^{th} power. The M^n -by-1 vector $\mathbf{c}_0^n(\tau_D^n)$ is the vector of nominal computed cross-correlations as defined in Eq. (27b) for the n^{th} signal. Its cross-correlation elements are computed using Eq. (24b) at the code delay offsets η_m^n for $m = 1, \dots, M^n$ and at the time delay τ_D^n . The M^n -by- $(3L_s)$ matrix $H^n(\tau_D^n)$ is the matrix of cross-correlation derivatives with respect to \mathbf{p} as defined in Eq. (28) for the n^{th} signal. Its cross-correlation derivative rows are computed using Eq. (24a) at the code delay offsets η_m^n for $m = 1, \dots, M^n$ and at the time delay τ_D^n . The M^n -by-1 vector $\tilde{\mathbf{c}}_{meas}^n$ is the vector of measured normalized cross-correlations as defined in Eq. (27a) for the n^{th} signal. Its measured cross-correlation elements are computed using Eqs. (9a)-(11) at the code delay offsets η_m^n for $m = 1, \dots, M^n$.

The unknown correlation amplitude loss factor A_c^n applies to the n^{th} signal. A unique value applies to each signal because of the uniqueness of each signal's wide-band autocorrelation function. Each different distorted cross-correlation shape can have a different loss of prompt correlation amplitude when filtered through $h(t; \mathbf{p})$.

There is an important reason that the vectors $\mathbf{c}_0^n(\tau_D^n)$ for $n = 1, \dots, N$ and the matrices $H^n(\tau_D^n)$ for $n = 1, \dots, N$ are modeled as having different delays τ_D^n for $n = 1, \dots, N$ that have the potential to vary with n . Recall from Subsection II.A that this delay is a measure of the time between the arrival of a particular PRN code chip at the input to the RF front-end and the time when its prompt replica is replayed by the DLL number controlled oscillator. This delay is unknown, but it can be guessed, and $h(t; \mathbf{p})$ can be estimated in a way that is self-consistent for purposes of predicting signal distortion according to the receiver's DLL-relative time base. There is one

caveat, though. The self-consistency of this calculation applies only to one signal at a time. For a given fixed $h(t; \mathbf{p})$, this delay may vary for different PRN codes. Such variations can be caused by the differing effects of coupling between the way that $h(t; \mathbf{p})$ distorts the PRN code's cross-correlation function and the way that the DLL discriminator operates on the distorted function to yield a code phase estimate or a proxy thereof.

Therefore, the multi-signal system identification procedure must allow for different delays of its different signals. The differential delays are estimated in an outer optimization that holds one of them fixed while varying the others in order to minimize the sum of the least-squares costs over all of the independent system-identification equations for all of the signals.

The set of evaluations of Eqs. (24a) and (24b) and the set of correlation measurement calculations in Eqs. (9a)-(11) for the n^{th} signal will involve the use of the PRN code for signal n , $Z^n(t)$ and its corresponding wide-band autocorrelation function $C_{ZZ}^n(\eta)$. The definitions of these functions must account for the average code Doppler shift of the signal and its effect on their nominal, un-Doppler-shifted versions. As per the discussion of after Eqs. (9a) and (9b), the Doppler-shifted versions of these functions are:

$$Z^n(t) = Z_{nom}^n[t(1 + \frac{\hat{\omega}_D^n}{\omega_c})] \text{ for } n = 1, \dots, N \quad (31a)$$

$$C_{ZZ}^n(\eta) = C_{ZZnom}^n[\eta(1 + \frac{\hat{\omega}_D^n}{\omega_c})] \text{ for } n = 1, \dots, N \quad (31b)$$

The functions $Z_{nom}^n[t]$ and $C_{ZZnom}^n[\eta]$ are the known nominal PRN code and autocorrelation functions, respectively, for the n^{th} signal, and $\hat{\omega}_D^n$ is its estimated carrier Doppler shift.

It is desirable to have significant frequency diversity among the N different Doppler shifts $\hat{\omega}_D^n$ for $n = 1, \dots, N$. Frequency diversity will increase the observability of the impulse response in the spectral regions near the PRN code power nulls. This will happen because frequency diversity will cause the nulls for the different signals to occur at different frequencies.

B. Penalty Terms to Favor Impulse Response Smoothness

The multi-signal system identification problem includes additional terms that penalize the third and fourth time derivatives of $h(t; \mathbf{p})$ at the mid points of the (L_s+1) spline intervals. These penalty terms take the form of additional equations in the over-determined system of equations:

$$0 = \frac{\Delta t_s^4}{4!} \sqrt{\frac{\rho_3 M_{tot}}{L_s + 1}} \frac{d^3 h}{dt^3} \Big|_{[(t_{sl} + 0.5\Delta t_s), \mathbf{p}]} \quad \text{for } l = 0, \dots, L_s \quad (32a)$$

$$0 = \frac{\Delta t_s^5}{5!} \sqrt{\frac{[\frac{25}{12} \rho_3 + \rho_4] M_{tot}}{L_s + 1}} \frac{d^4 h}{dt^4} \Big|_{[(t_{sl} + 0.5\Delta t_s), \mathbf{p}]} \quad \text{for } l = 0, \dots, L_s \quad (32b)$$

where the positive constants ρ_3 and ρ_4 provide a way of tuning the weights of these penalty terms in the overall sum-squared-error cost function. The quantity $M_{tot} = M^1 + M^2 + \dots + M^N$ is the total number of code-phase offsets whose cross-correlation measurements are considered for the N signals.

The complicated factors in front of the two $h(t; \mathbf{p})$ time derivatives in Eqs. (32a) and (32b) are reasonable normalizing terms. They allow for an "apples-to-apples" comparison between correlation errors in Eq. (30), third time derivatives of $h(t; \mathbf{p})$ in Eq. (32a), and fourth time derivatives in Eq. (32b).

The final system identification problem appends Eqs. (32a) and (32b) to the system of equations whose sum-squared-error cost function is minimized. The inclusion of these terms acts to reduce the high-frequency oscillations of $h(t; \mathbf{p})$. Higher weighting values ρ_3 and ρ_4 will tend to smooth out any roughness on the estimated $h(t; \mathbf{p})$, but at the possible expense of degraded fit to the correlation relationship in Eq. (7).

The spline model of $h(t; \mathbf{p})$ in Eq. (18) can be used to express the third and fourth derivatives in Eqs. (32a) and (32b) in forms that are linear in \mathbf{p} :

$$\begin{aligned} \frac{d^3 h}{dt^3} \Big|_{[(t_{sl} + 0.5\Delta t_s), \mathbf{p}]} &= \frac{d^3 h}{dt^3} \Big|_{[(t_{sl} + 0.5\Delta t_s), 0]} \\ &+ \left[\frac{\partial(d^3 h/dt^3)}{\partial \mathbf{p}} \Big|_{(t_{sl} + 0.5\Delta t_s)} \right] \mathbf{p} \end{aligned} \quad \text{for } l = 0, \dots, L_s \quad (33a)$$

$$\begin{aligned} \frac{d^4 h}{dt^4} \Big|_{[(t_{sl} + 0.5\Delta t_s), \mathbf{p}]} &= \frac{d^4 h}{dt^4} \Big|_{[(t_{sl} + 0.5\Delta t_s), 0]} \\ &+ \left[\frac{\partial(d^4 h/dt^4)}{\partial \mathbf{p}} \Big|_{(t_{sl} + 0.5\Delta t_s)} \right] \mathbf{p} \end{aligned} \quad \text{for } l = 0, \dots, L_s \quad (33b)$$

These formulas are similar to the linear-in- \mathbf{p} formula for $h(t; \mathbf{p})$ given in Eq. (21). The formulas for each term in Eqs. (33a) and (33b) can be derived by appropriate differentiation of the spline formula in Eq. (18), much as Eq. (21) has been derived from Eq. (18). The details of

this derivation have been omitted for the sake of brevity.

The $2(L_s+1)$ individual penalty formulas in Eqs. (32a) and (32b) can be combined with the linear model forms in Eqs. (33a) and (33b) in order to produce a system of penalty equations of the form:

$$0 = \mathbf{c}_{pen} + H_{pen} \mathbf{p} \quad (34)$$

where \mathbf{c}_{pen} is the column vector of dimension $2(L_s+1)$:

$$\mathbf{c}_{pen} = \frac{\Delta t_s^4}{4!} \sqrt{\frac{M_{tot}}{L_s + 1}} \times \begin{bmatrix} \sqrt{\rho_3} \frac{d^3 h}{dt^3} \Big|_{[(t_{s0} + 0.5\Delta t_s), 0]} \\ \vdots \\ \sqrt{\rho_3} \frac{d^3 h}{dt^3} \Big|_{[(t_{sL_s} + 0.5\Delta t_s), 0]} \\ \frac{\Delta t}{5} \sqrt{\frac{25}{12} \rho_3 + \rho_4} \frac{d^4 h}{dt^4} \Big|_{[(t_{s0} + 0.5\Delta t_s), 0]} \\ \vdots \\ \frac{\Delta t}{5} \sqrt{\frac{25}{12} \rho_3 + \rho_4} \frac{d^4 h}{dt^4} \Big|_{[(t_{sL_s} + 0.5\Delta t_s), 0]} \end{bmatrix} \quad (35)$$

and H_{pen} is the matrix of dimension $2(L_s+1)$ -by- $(3L_s)$:

$$H_{pen} = \frac{\Delta t_s^4}{4!} \sqrt{\frac{M_{tot}}{L_s + 1}} \times \begin{bmatrix} \sqrt{\rho_3} \frac{\partial(d^3 h/dt^3)}{\partial \mathbf{p}} \Big|_{(t_{s0} + 0.5\Delta t_s)} \\ \vdots \\ \sqrt{\rho_3} \frac{\partial(d^3 h/dt^3)}{\partial \mathbf{p}} \Big|_{(t_{sL_s} + 0.5\Delta t_s)} \\ \frac{\Delta t}{5} \sqrt{\frac{25}{12} \rho_3 + \rho_4} \frac{\partial(d^4 h/dt^4)}{\partial \mathbf{p}} \Big|_{(t_{s0} + 0.5\Delta t_s)} \\ \vdots \\ \frac{\Delta t}{5} \sqrt{\frac{25}{12} \rho_3 + \rho_4} \frac{\partial(d^4 h/dt^4)}{\partial \mathbf{p}} \Big|_{(t_{sL_s} + 0.5\Delta t_s)} \end{bmatrix} \quad (36)$$

C. Combined Linear Least-Squares Problem Formulation with Penalty Terms

The cross-correlation measurement models for the N signals in Eq. (30) and the penalty terms in Eq. (34) can be combined into the following over-determined system of linear equations:

$$\begin{bmatrix} -\mathbf{c}_0^1(\tau_D^1) \\ -\mathbf{c}_0^2(\tau_D^2) \\ \vdots \\ -\mathbf{c}_0^N(\tau_D^N) \\ -\mathbf{c}_{pen} \end{bmatrix} = \begin{bmatrix} H^1(\tau_D^1) & -\tilde{\mathbf{c}}_{meas}^1 & 0 & \dots & 0 \\ H^2(\tau_D^2) & 0 & -\tilde{\mathbf{c}}_{meas}^2 & \dots & 0 \\ \vdots & \vdots & \vdots & \ddots & \vdots \\ H^N(\tau_D^N) & 0 & 0 & \dots & -\tilde{\mathbf{c}}_{meas}^N \\ H_{pen} & 0 & 0 & \dots & 0 \end{bmatrix} \begin{bmatrix} \mathbf{p} \\ A_c^1 \\ A_c^2 \\ \vdots \\ A_c^N \end{bmatrix} \quad (37)$$

This is a system of $M_{tot}+2(L_s+1)$ equations in the $3L_s+N$ unknown elements of the vector $[\mathbf{p}; A_c^1; A_c^2; \dots; A_c^N]$. If there are enough cross-correlation time offsets to yield an over-determined system identification problem for each signal taken individually, then each M^n value is greater than $3L_s+1$. In this case $M_{tot} > 3L_s+N$ also holds true, the above problem will be over-determined, and it would have been over-determined even if there had been no penalty terms on the third and fourth time derivatives of $h(t; \mathbf{p})$.

The unknown vector $[\mathbf{p}; A_c^1; A_c^2; \dots; A_c^N]$ can be estimated by solving Eq. (37) using standard linear least-square matrix calculations⁷. As with the least-squares problems for the individual signals, the solution calculations must be able to handle complex arithmetic properly because the measured $\tilde{\mathbf{c}}_{meas}^n$ vectors will be complex. The solution vector $[\mathbf{p}; A_c^1; A_c^2; \dots; A_c^N]$ will also be complex.

The minimum least-squares cost associated with Eq. (37) equals half the sum of the squares of the absolute values of the errors in each scalar equation. This cost will be a function of the chosen delays for the signals. Let this cost be $J_{opt}(\tau_D^1, \tau_D^2, \dots, \tau_D^N)$. This will be a scalar, non-negative, real number for a given set of delays.

D. Outer Optimization of Differential Signal Delays

The system identification procedure must estimate $N-1$ of the delays $\tau_D^1, \tau_D^2, \dots$, and τ_D^N in addition to the spline coefficients in \mathbf{p} and the correlation amplitude loss factors $A_c^1, A_c^2, \dots, A_c^N$. This is true because only one of the delays is independent. Without loss of generality, τ_D^1 is held fixed at an a priori assigned value, and the values of $\tau_D^2, \dots, \tau_D^N$ are estimated by choosing the combination of these delays that minimizes $J_{opt}(\tau_D^1, \tau_D^2, \dots, \tau_D^N)$.

The underlying problem of estimating $\tau_D^2, \dots, \tau_D^N$ is a non-linear problem because the τ_D^n values do not enter the problem model in Eq. (37) linearly. Therefore, the

method used to minimize $J_{opt}(\tau_D^1, \tau_D^2, \dots, \tau_D^N)$ is Newton's method, which is appropriate for nonlinear problems⁷.

Newton's method requires a first guess of the solution, and it computes improved guesses by using the gradient and Hessian of J_{opt} at its current guess. The estimation procedure initializes its guess by setting all of the estimated delays to the pre-defined value for signal 1: $\tau_D^n = \tau_D^1$ for $n = 2, \dots, N$. It then uses the finite-difference increment $\delta\tau_D$ and central differencing in order approximate the gradient and Hessian components:

$$\begin{aligned} \frac{\partial J_{opt}}{\partial \tau_D^n} &\cong \{J_{opt}[\tau_D^1, \dots, (\tau_D^n + \delta\tau_D), \dots, \tau_D^N] \\ &\quad - J_{opt}[\tau_D^1, \dots, (\tau_D^n - \delta\tau_D), \dots, \tau_D^N]\} / (2\delta\tau_D) \\ &\quad \text{for } n = 2, \dots, N \end{aligned} \quad (38a)$$

$$\begin{aligned} \frac{\partial^2 J_{opt}}{\partial (\tau_D^n)^2} &\cong \{J_{opt}[\tau_D^1, \dots, (\tau_D^n + \delta\tau_D), \dots, \tau_D^N] \\ &\quad + J_{opt}[\tau_D^1, \dots, (\tau_D^n - \delta\tau_D), \dots, \tau_D^N] \\ &\quad - 2J_{opt}[\tau_D^1, \dots, \tau_D^n, \dots, \tau_D^N]\} / \delta\tau_D^2 \\ &\quad \text{for } n = 2, \dots, N \end{aligned} \quad (38b)$$

$$\begin{aligned} \frac{\partial^2 J_{opt}}{\partial \tau_D^l \partial \tau_D^n} &\cong \\ &\{J_{opt}[\tau_D^1, \dots, (\tau_D^l + \delta\tau_D), \dots, (\tau_D^n + \delta\tau_D), \dots, \tau_D^N] \\ &\quad + J_{opt}[\tau_D^1, \dots, (\tau_D^l - \delta\tau_D), \dots, (\tau_D^n - \delta\tau_D), \dots, \tau_D^N] \\ &\quad - J_{opt}[\tau_D^1, \dots, (\tau_D^l - \delta\tau_D), \dots, (\tau_D^n + \delta\tau_D), \dots, \tau_D^N] \\ &\quad - J_{opt}[\tau_D^1, \dots, (\tau_D^l + \delta\tau_D), \dots, (\tau_D^n - \delta\tau_D), \dots, \tau_D^N]\} \times \\ &\quad [1/(2\delta\tau_D)^2] \\ &\quad \text{for } l = 2, \dots, (N-1) \text{ and } n = (l+1), \dots, N \end{aligned} \quad (38c)$$

One must be careful to choose the finite-difference step size $\delta\tau_D$ wisely. If it is too large, then these approximations will be poor due to truncation error, but they will have too much error due to computer round-off if $\delta\tau_D$ is too small⁷.

These second derivative calculations require $2(N-1)^2$ extra evaluations of $J_{opt}(\tau_D^1, \tau_D^2, \dots, \tau_D^N)$ at various combinations of 1 or 2 perturbed values of the quantities $\tau_D^2, \dots, \tau_D^N$. Each such evaluations requires a solution of the linear least-squares parameter identification problem in Eq. (37). Fortunately, each linear solution can be computed quickly because it involves only standard linear algebra. Therefore, the finite-difference computations in Eqs. (38a)-(38c) are practical.

Increments to the delay estimates are computed using the

standard Newton's method formula:

$$\begin{bmatrix} \Delta \tau_D^2 \\ \Delta \tau_D^2 \\ \vdots \\ \Delta \tau_D^N \end{bmatrix} = - \begin{bmatrix} \frac{\partial^2 J_{opt}}{\partial(\tau_D^2)^2} & \frac{\partial^2 J_{opt}}{\partial(\tau_D^2)\partial(\tau_D^3)} & \cdots & \frac{\partial^2 J_{opt}}{\partial(\tau_D^2)\partial(\tau_D^N)} \\ \frac{\partial^2 J_{opt}}{\partial(\tau_D^2)\partial(\tau_D^3)} & \frac{\partial^2 J_{opt}}{\partial(\tau_D^3)^2} & \cdots & \frac{\partial^2 J_{opt}}{\partial(\tau_D^3)\partial(\tau_D^N)} \\ \vdots & \vdots & \ddots & \vdots \\ \frac{\partial^2 J_{opt}}{\partial(\tau_D^2)\partial(\tau_D^N)} & \frac{\partial^2 J_{opt}}{\partial(\tau_D^3)\partial(\tau_D^N)} & \cdots & \frac{\partial^2 J_{opt}}{\partial(\tau_D^N)^2} \end{bmatrix}^{-1} \begin{bmatrix} \frac{\partial J_{opt}}{\partial(\tau_D^2)} \\ \frac{\partial J_{opt}}{\partial(\tau_D^3)} \\ \vdots \\ \frac{\partial J_{opt}}{\partial(\tau_D^N)} \end{bmatrix} \quad (39)$$

These increments are added to existing estimates to produce the new estimates:

$$(\tau_D^n)_{new} = \tau_D^n + \Delta \tau_D^n \quad \text{for } n = 2, \dots, N \quad (40)$$

The process is repeated as needed until the increments $\Delta \tau_D^n$ for $n = 2, \dots, N$ are negligible. In the authors' experience, the initial guesses of $\tau_D^2, \dots, \tau_D^N$ are normally close to the optimal values, and only one iteration of this procedure is needed in order to achieve accurate delay estimates.

V. EXPERIMENTAL APPLICATION AND RESULTS FOR TWO NARROW-BAND RF FRONT-ENDS

A. Cases Considered and Their Input Parameters

The system identification calculations of this paper have been applied to two different RF front-end designs. One is the Zarlink/Plessey GP2015⁸. The other is custom-designed RF front-end. Both of them are narrow-band GPS L1 RF front-ends. Their filters have bandwidths on the order of 2 MHz wide in order to capture the main lobe of the GPS C/A code, and they both produce 2-bit RF samples at the sampling frequency 5.714 MHz. System identification experiments and calculations have been carried out for two units of each design.

The system identification procedure started by collecting raw RF samples and storing them to disk. The data were collected in Sept. 2010 using roof-mounted antennas. Three of the RF front-ends and digital storage devices were located in Ithaca, NY. One of the custom-designed units was located in Austin, TX. The two Zarlink/Plessey RF front-ends collected data at the same time. The two custom-designed RF front-ends also collected data simultaneously, but at a different time than the Zarlink/Plessey units.

Signal acquisition and tracking operations for a number of GPS C/A PRN codes were carried out using MATLAB

software receiver code on an off-line basis. These tracking results were used to compute normalized cross-correlation measurements as per Eqs. (9a)-(11). All four system identification cases computed cross-correlation measurements using data batches of 91 seconds duration.

For each signal, $M^n = 341$ η_m offsets that range from -5 C/A code chips to +5 C/A code chips. Three different spacings were used between the η_m offsets. Spacings of $\eta_{m+1} - \eta_m$ were set to 0.05 chips for $|\eta_m|$ in the range 2 to 5 chips, to 0.02 chips for $|\eta_m|$ in the range 0.2 to 2 chips, and to 0.01 chips for $|\eta_m| < 0.2$ chips. Thus, the finest spacing was used near the cross-correlation peak at $\eta = 0$.

The maximum non-zero durations used for the two different RF front-end's impulse responses were $t_{max} = 5.65$ μsec for the Zarlink/Plessey devices and $t_{max} = 2.90$ μsec for the custom devices. The shorter duration for the latter RF front-end was deemed reasonable given its somewhat higher bandwidth. The preset delays were chosen to be $\tau_D^1 = 2.13$ μsec for the Zarlink/Plessey RF front-ends and $\tau_D^1 = 0.78$ μsec for the custom RF front-ends. The finite-difference increments used to compute derivatives with respect to $\tau_D^2, \dots, \tau_D^N$ in the outer Newton optimization were $\delta\tau_D = 5.65$ nsec for the Zarlink/Plessey units and $\delta\tau_D = 2.90$ nsec for the custom units.

The following values were used for the smoothness-inducing penalty weights of Eqs. (32a)-(36): $\rho_3 = 1000$ and $\rho_4 = 100$. These values were use for both RF front-end types.

The number of spline intervals used for all cases was $L_s + 1 = 21$. Thus, there were $3L_s = 60$ elements in the unknown \mathbf{p} vector.

The system identification calculations for the Zarlink/Plessey RF front-ends used $N = 3$ signals, those of PRN numbers 08, 11, and 28. The total number of cross-correlation measurements was $M_{tot} = 3 \times 341 = 1023$ for these cases, and each over-determined linear least-squares problem in Eq. (37) consisted of 1065 equations in 63 unknowns. Thus, the parameter identification problem was highly over-determined. The respective average carrier Doppler shifts for PRNs 08, 11, and 28 were 265 Hz, 1517 Hz, and 2052 Hz for one of the Zarlink/Plessey cases and -426 Hz, 825 Hz, and 1362 Hz for the other case. Thus, there was some Doppler diversity, but not as much as might be had for a terrestrial receiver.

The system identifications calculations for the custom front-ends used signals from the $N = 4$ PRN numbers: 04, 08, 17, and 28. $M_{tot} = 4 \times 341 = 1364$, and each system identification problem consisted of 1406 equations in 64 unknowns, which was even more over-determined than

for the Zarlink/Plessey RF front-ends. These four PRN codes' corresponding carrier Doppler shifts were 3572 Hz, -3826 Hz, 913 Hz, and -509 Hz for one case and 3000 Hz, -3426 Hz, -654 Hz, and -329 Hz for the other case. Thus, the cases for the custom RF front-end have significantly more Doppler shift diversity than those for the Zarlink/Plessey front-end.

B. Impulse Response Data and Results

Example correlation measurement data for PRN 08 and a Zarlink/Plessey RF front-end are shown in Fig. 3. The figure plots $A_c \tilde{C}_{ZZ}(\eta)$ vs. η with A_c being the value that has been computed in a subsequent system identification calculation. The real part of $A_c \tilde{C}_{ZZ}(\eta)$ is the dash-dotted red curve, and the imaginary part of $A_c \tilde{C}_{ZZ}(\eta)$ is the dashed green curve. Also shown in the figure is the theoretical wide-band autocorrelation function for this signal, $C_{ZZ}(\eta)$, which is the solid blue curve. The system identification problem defined by Eq. (7) is to find the complex $h(t)$ function that, when used to evaluate the right-hand side of the equation in conjunction with the given solid blue $C_{ZZ}(\eta)$ plot in Fig. 3, yields the other two plots in the figure. If the receiver had a very wide bandwidth, then $h(t)$ would be approximately a Dirac delta function, the dash-dotted red curve would closely approximate the solid blue curve, and the dashed green curve would be nearly zero. Figure 3 shows that this is not the case, but it also shows that the filter bandwidth is wide enough so that the red and green curves are not terrible approximations of the wide-band case. This level of distortion of the narrow-band cross-correlation function is representative of all the data sets.

Figure 4 shows an example of the fit between the measured cross-correlation function and its corresponding modeled value from Eq. (7) after estimation of $h(t; \mathbf{p})$. These plots are for PRN 28 and the custom-designed RF front-end. The solid red curve in the figure is the measured real part of $A_c \tilde{C}_{ZZ}(\eta)$, and the solid green curve is the measured imaginary part. The dotted turquoise curve is the real part of the modeled $C_{ZZ}(\eta)$ as computed using $h(t; \mathbf{p})$ with the estimated \mathbf{p} in Eq. (7). The dotted grey curve is the imaginary part of the modeled $C_{ZZ}(\eta)$. As is obvious from the figure, the two modeled curves lie right on top of the measured curves. The dash-dotted brown curve plots the error absolute value $|C_{ZZ}(\eta) - A_c \tilde{C}_{ZZ}(\eta)|$. It is nearly zero. Its maximum value is 0.003, which is only 0.33 % of the maximum cross-correlation. Thus, this system identification model fit is very accurate.

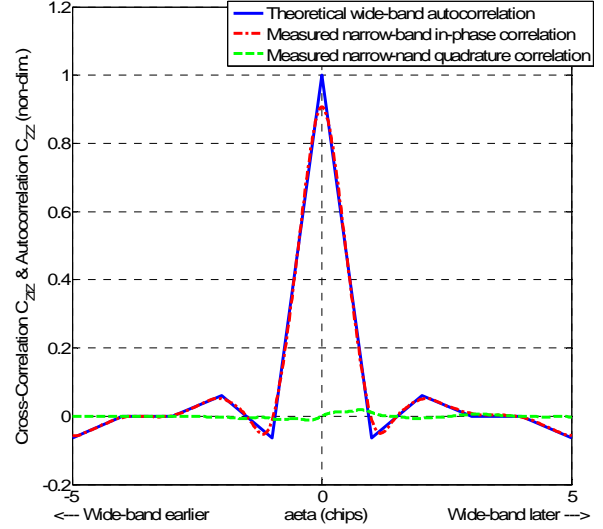


Fig. 3. Measured cross-correlation data for PRN 08 as received by a Zarlink/Plessey RF front-end along with theoretical wide-band autocorrelation.

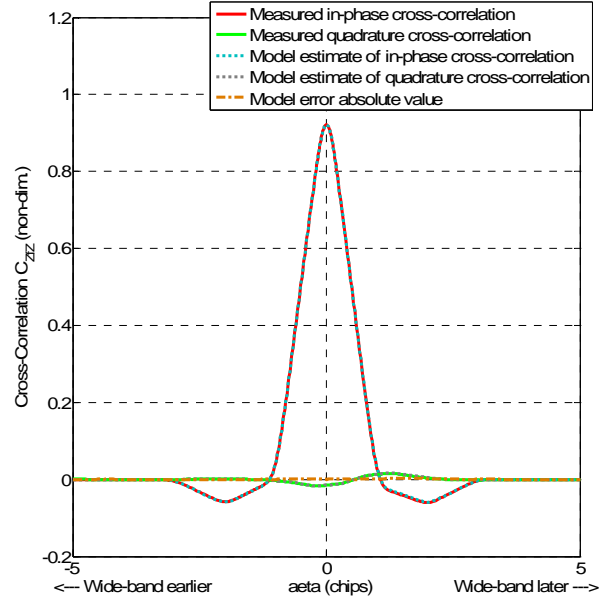


Fig. 4. Measured and estimated cross-correlation functions for PRN 28 as received by a custom-designed RF front-end along with absolute values of estimation error residuals.

The fit accuracy of Fig. 4 is typical of all cases that have been processed. The maximum fit error maximized over all the cases and all η values was 0.77% of the corresponding peak cross-correlation. Root Mean Square (RMS) fit errors were all in the range 0.09% to 0.29% of the peak cross-correlation. These good fits indicate that the method works well, especially when one considers that these close fits occur with a single estimated $h(t; \mathbf{p})$

impulse response function accounting for the shapes of 3 or 4 different distorted cross-correlation functions.

It is interesting to note that RMS errors for positive η were uniformly larger than those for negative η values. Averaged over all 14 measured cross-correlation cases, the RMS errors in the $-\eta$ range are only 46% of those in the $+\eta$ range. Given that the $+\eta$ range corresponds to late correlations, this is consistent with the idea that part of this discrepancy is caused by multi-path because multi-path errors should be larger in this region. Given the good simultaneous fits for 3 to 4 signals that arrived along 3 to 4 independent lines of sight, one suspects that the multi-path effects on each $h(t;\mathbf{p})$ estimate are small. Also, it is reasonable to expect that the averaging across signals inherent in this procedure will tend to reduce multi-path errors in $h(t;\mathbf{p})$ further.

The estimated inter-channel time offsets, $\tau_D^n - \tau_D^1$ for $n = 2, \dots, N$, were all small. They ranged from -0.76 nsec to $+1.04$ nsec.

The estimated $h(t;\mathbf{p})$ impulse response functions for the 4 system parameter identification cases are plotted in Fig. 5. The upper panel plots the impulse responses for the two Zarlink/Plessey units. The lower panel plots them for the two custom-designed units. Both real and imaginary parts are plotted. Both plots show the entire non-zero portions of the corresponding finite responses. Both sets of curves show the functions settling down to near zero at both ends of each non-zero range. This indicates that the choices of t_{max} and τ_D^1 provided adequate margins to capture the important variations of the functions. Another interesting feature of these plots is the close similarity between the two units of each design, especially the real parts: Note how the dotted red curves in each panel, the real parts for unit B of the given design, closely match the solid blue curves, the real parts for unit A of the same design.

Another interesting feature of Fig. 5 is the close alignment of the real-part peaks with the corresponding pre-specified τ_D^1 delays. Recall that these values are $\tau_D^1 = 2.13$ μsec for the upper Zarlink/Plessey plot and $\tau_D^1 = 0.78$ μsec for the lower custom-design plot. This seems sensible because τ_D^1 is defined to be the nominal delay from when the prompt code enters the RF front-end's analog input to when the code appears in its output sample stream.

The frequency-response gains of the estimated envelop impulse response functions are plotted in Fig. 6. The frequency response transfer function is computed from the impulse response function as follows

$$G(j\omega) = \int_0^{\infty} h(t;\mathbf{p})e^{-j\omega t} dt = \int_0^{t_{max}} h(t;\mathbf{p})e^{-j\omega t} dt \quad (41)$$

where $j = \sqrt{-1}$ in this equation. This integral can be evaluated exactly because $h(t;\mathbf{p})$ is quartic in t over each of the L_s+1 spline intervals and because functions of the form $t^n \cos(\alpha t)$ and $t^n \sin(\alpha t)$ can be integrated in closed form for any integers n . Figure 6 plots $20\log_{10}|G(j\omega)|$ vs. ω for the 4 estimated impulse response functions. Note how each plot passes through 0 dB at the center frequency. This feature is a consequence of the unit-normalization constraint in Eq. (14).

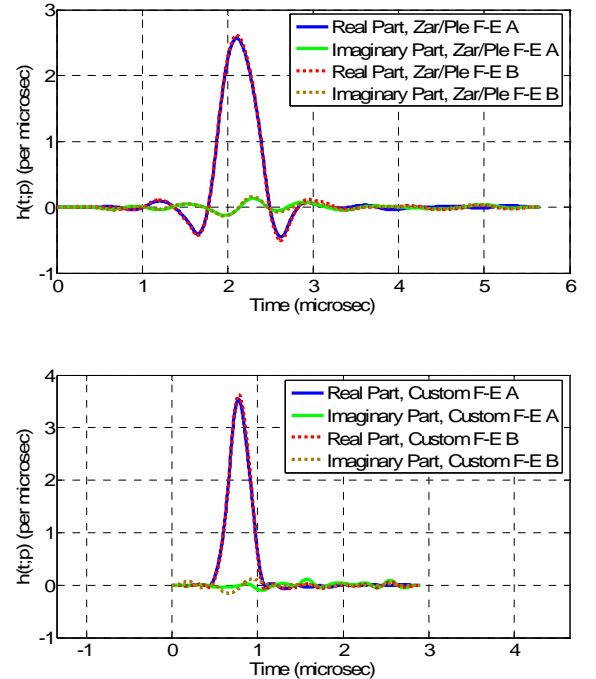


Fig. 5. Estimated envelop impulse response functions for 4 RF front-ends: two Zarlink/Plessey units (top plot) and two custom-designed units (bottom plot).

The plots in Fig. 6 have been compared with the RF filter frequency response plots that have been provided by the relevant manufacturers, e.g., see Ref. 8. Both sets of plots in the figure agree reasonably well with the manufacturers' data sheets. This agreement further confirms the efficacy of the new filter system identification method.

A counter-intuitive aspect of Fig. 6 is the apparent accuracy of the frequency response plots at certain frequencies. The vertical dash-dotted brown lines are plotted at ± 1.023 MHz. These are the nominal points of the first nulls of the C/A code power spectrum. If using the methods of Refs. 4 or 5, one would expect large

frequency response errors near these frequencies, but the curves shown in Fig. 6 match the manufacturer data reasonably well in these regions. This good performance of the estimator is probably the result of two features of the new system identification method. First, the use of a time-domain spline model of the impulse response should tend to generate a smooth frequency response function in regions of the spectrum where the input signal is weak. Second, the frequency diversity caused by code Doppler shift avoids the possibility of a complete lack of input signal power at any one frequency.

The second counter-intuitive aspect of Fig. 6 is the apparent ability to resolve the correct frequency response at frequencies outside the Nyquist aliasing band. The Nyquist bandwidth equals half the RF sampling frequency of 5.714 MHz², and it is centered on the plot. The Nyquist band is the set of frequencies between the dashed green vertical lines on the plot. Again, based on comparisons with manufacturer's data sheets, the frequency response curves in Fig. 6 seem reasonable in areas outside this Nyquist zone, though the low gains far outside this zone make all estimates, both these and the manufacturers', suspect. Nevertheless, it seems surprising that the new method has any ability to resolve the frequency response outside the Nyquist band. It is conjectured that this ability is a result of the fact that the RF sampling frequency is not an integer multiple of the C/A-code chipping frequency. This unusual relationship and the fact that the input signal has known wide-bandwidth frequency characteristics may enable the system identification algorithm to circumvent the issue of aliasing.

Another important result of the present paper has been the ability to use its estimated $h(t;\mathbf{p})$ impulse response functions in support of semi-codeless P(Y) signal processing in a spoofing detection application¹. The goal in this case is to model the distortion caused by $h(t;\mathbf{p})$ on groups of about 20 actual known P code chips. Each group corresponds to a single one of the encryption chips that modulate the P code to create the P(Y) code. Figure 7 shows examples of this type of distortion calculation for one of this paper's custom RF front-end $h(t;\mathbf{p})$ estimates. The lower distorted curves in the figure are derived from the upper wide-band sets of P-code chips by using the estimated $h(t;\mathbf{p})$ response function in Eq. (3). The $Z(t)$ functions input on the right-hand side of the Eq. (3) calculation are the wide-band $P_{w\mathbf{y}}(t)$ P-chip profiles shown in the upper panel of the figure. The $Z_f(t)$ functions that are output on the left-hand side of Eq. (3) are the corresponding distorted $P_{f\mathbf{w}\mathbf{y}}(t)$ functions in the lower panel of Fig. 7.

Of course, generation of a set of distorted $P_{f\mathbf{w}\mathbf{y}}(t)$ functions is not a proof that the $h(t;\mathbf{p})$ used to generate them is an accurate model of the actual narrow-band RF filter. The evidence for the accuracy of the various $h(t;\mathbf{p})$ estimates

lies, rather, in the success of the semi-codeless spoofing detection test that has been developed based on them. Reference 1 demonstrates good agreement between the predicted mean and variance of its semi-codeless spoofing detection statistic on the one hand and its experimentally determined fluctuations on the other hand. It seems unlikely that this level of agreement could have been achieved based on poor $h(t;\mathbf{p})$ estimates.

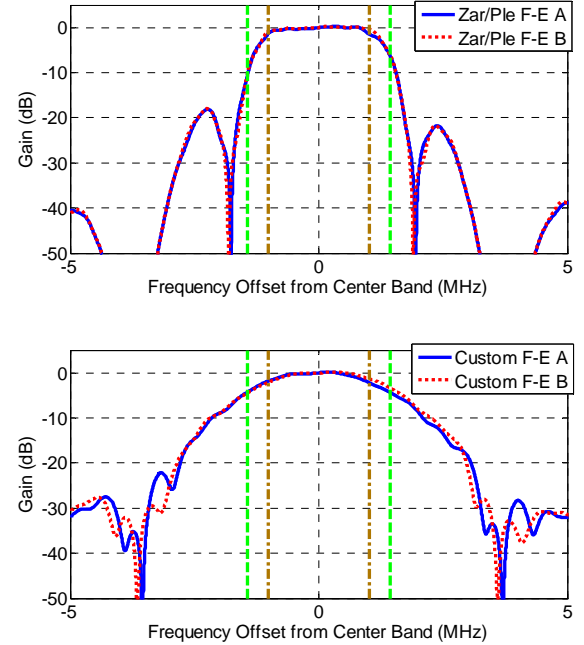


Fig. 6. Estimated frequency responses for 4 RF front-ends: two Zarlink/Plessey units (top plot) and two custom-designed units (bottom plot).

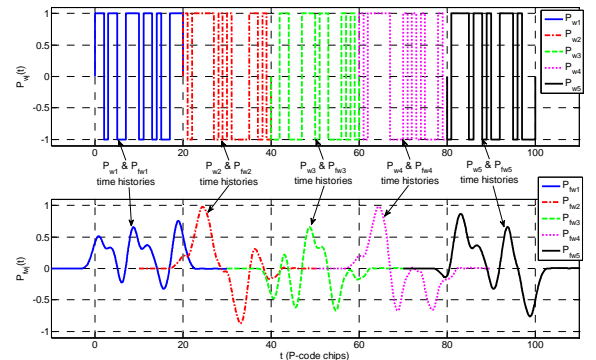


Fig. 7. Wide-band (top) and filtered (bottom) P-code chips of 5 successive W encryption chips, distortion modeled by the $h(t;\mathbf{p})$ function for one of the custom-designed RF front-ends (courtesy of Ref. 1).

VI. SUGGESTIONS FOR FURTHER STUDY

Although the results of Section V are encouraging, there remain some open questions about this technique. They all revolve around the effects of noise and other possible limits on its accuracy. One worthwhile study would be to model the effects of receiver-noise-induced random errors in the measured accumulations $\tilde{C}_{ZZ}(\eta)$. Standard linearization techniques could be used to propagate these effects through the system identification calculations. The result would be an estimation error covariance matrix for the spline parameter vector \mathbf{p} . This estimation error covariance could be propagated through the frequency response calculations in order to determine whether there are frequency ranges with poor estimation accuracy. This calculation would shed light on the two questions associated with Fig. 6: How much frequency response uncertainty exists near the C/A code power nulls? Does accuracy degrade outside the Nyquist bandwidth because of aliasing?

A second test of the issue of aliasing could try estimating $h(t;\mathbf{p})$ from truth-model simulation data. The "truth" $h(t;\mathbf{p})$ would be given significant main-lobe gain and some side-lobes outside the Nyquist band. If the estimated $h(t;\mathbf{p})$ were able to reproduce these features of the "truth" $h(t;\mathbf{p})$, then the question of Nyquist limitations would be settled.

Another issue concerns the effect of multi-path on the accuracy of $h(t;\mathbf{p})$. The heuristic strategy of using multiple signals in one large system identification calculation has been employed in hopes of reducing the multi-path effects on the estimated $h(t;\mathbf{p})$. No analysis of the efficacy of this approach has been conducted. Such an analysis should be carried out.

VII. SUMMARY AND CONCLUSIONS

A new system identification method has been developed to estimate the envelop impulse response function of an RF front-end filter. This method estimates the node coefficients of a complex time-domain impulse response function that takes the form of a 4th-order spline. The estimation problem definition relies on measurements of the distorted cross-correlation function between an original wide-band PRN code and its received version. This cross-correlation function is calculated at many code-phase shifts relative to the prompt code of a receiver's DLL, perhaps hundreds of phase shifts spread over 5 to 10 code chips. The distorted cross-correlation function is modeled as being the convolution between the unknown impulse response function and the known autocorrelation function for the undistorted wide-band version of the PRN code. The resulting system-

identification problem is linear in almost all of its unknowns, and it can be formulated to use data from multiple PRN codes simultaneously.

The new method has been applied experimentally in an off-line mode to calibrate the impulse response functions of two narrow-band RF front-end designs. These designs are geared for reception of the GPS L1 C/A code. The system identification results showed good agreement between multiple signals for a single impulse response model in a given receiver. Corresponding frequency response functions have been computed from the estimated impulse responses, and they agree favorably with experimental gain plots from manufacturer data sheets. As a further testimony to the fidelity of the estimated impulse responses, they have been successfully applied to develop a spoofing detection system that relies on semi-codeless matched-filter processing of P(Y) code signals in a narrow-band receiver.

ACKNOWLEDGMENT

Jahshan A. Bhatti, a Ph.D. candidate in the Department of Aerospace Engineering & Engineering Mechanics at UT Austin, helped to collect some of the data that have been used in this study. His research advisor, Prof. Todd E. Humphreys, supported his efforts on behalf of this project.

REFERENCES

1. Psiaki, M.L., O'Hanlon, B.W., Bhatti, J.A., Shepard, D.P, and Humphreys, T.E., "Civilian GPS Spoofing Detection based on Dual-Receiver Correlation of Military Signals," *Proc. ION GNSS 2011*, Sept. 20-23, 2011, Portland, OR.
2. Couch, L.W., *Digital and Analog Communication Systems*, 4th Edition, Macmillan, (New York, 1993), pp. 245-251.
3. Yang, C., and Miller, M., "Novel GNSS Receiver Design Based on Satellite Signal Channel Transfer Function/Impulse Response," *Proc. ION GNSS 2005*, Sept. 13-16, 2005, Long Beach, CA, pp. 1103-1115.
4. Pratt, A.R., "Performance Limits of Multi-Path Mitigation for Short Delay," *Proc. ION GNSS 2006*, Sept. 26-29, 2006, Fort Worth, TX, pp. 1723-1732.
5. Yang, C., Nguyen, T., and Miller, M., "GNSS Signal Channel Impulse Response Estimation: Modified Inverse Filter vs. Wiener Filter," *Proc. ION GNSS 2009*, Sept. 22-25, 2009, Savannah, GA, pp. 295-303.
6. Yang, C., "Global Navigation Satellite System (GNSS) Receivers Based on Satellite Signal Channel Impulse Response," U.S. Patent No. 7,471,241, Dec. 2008.
7. Gill, P.E., Murray, W., and Wright, M.H., *Practical Optimization*, Academic Press, (New York, 1981), pp. 37-40, 54-56, 105-106, 115-116, 127-131.

8. Anon., "GP2015 Global Positioning System Receiver RF Front End," *Global Positioning Products Handbook*, GEC Plessey Semiconductors, Wiltshire, U.K., 1996, pp. 49-63.